Desalination and Water Treatment
www.deswater.com

doi: 10.5004/dwt.2021.27363

229 (2021) 362–371
July

Generalized RBF artificial neural network applied to a reactive dyes photodiscoloration prediction problem

Leda Maria Saragiotto Colpini[a,b,*], Rodrigo Clemente Thom de Souza[a,c,d], Giane Gonçalves Lenzi[b], Raphael Menechini Neto[e], Onélia Aparecida Andreo dos Santos[e], Luiz Mário de Matos Jorge[e], Mateus Barbian Urio[f], Helton José Alves[f]

[a]*Universidade Federal do Paraná – Campus Avançado de Jandaia do Sul, Rua Doutor João Maximiano 426, Centro, 86900-000, Jandaia do Sul – PR, Brazil, Tel. + 55 (41) 3208-6190; emails: ledasaracol@ufpr.br (L.M.S. Colpini), thom@ufpr.br (R.C.T. Souza)*
[b]*Universidade Tecnológica Federal do Paraná, Av. Monteiro Lobato, s/n – Km 04, 84016-210, Ponta Grossa – PR, Brazil, email: gianeg@utfpr.edu.br*
[c]*Universidade Estadual de Maringá – Programa de Pós-Graduação em Ciência da Computação, Av. Colombo, 5790, 87020-900 – Maringá - PR, Brazil*
[d]*Universidade Estadual de Maringá – Programa de Pós-Graduação em Engenharia de Produção, Av. Colombo, 5790, 87020-900 – Maringá - PR, Brazil*
[e]*Universidade Estadual de Maringá – Departamento de Engenharia Química, Av. Colombo, 5790, 87020-900 – Maringá – PR, Brazil, emails: menechini@gmail.com (R.M. Neto), onelia@deq.uem.br (O.A.A. Santos), lmmj@deq.uem.br (L.M.M. Jorge)*
[f]*Universidade Federal do Paraná, Setor Palotina, Rua Pioneiro 2153, Jardim Dallas, 85950-000, Palotina – PR, Brazil, emails: mateusurio@gmail.com (M.B. Urio), helton.alves@ufpr.br (H.J. Alves)*

Received 25 November 2020; Accepted 18 April 2021

ABSTRACT

This study describes the application of TiO_2, Fe/TiO_2 and Ni/TiO_2 (2 and 5% wt) using the sol-gel method for the reactive dyes discoloration under artificial and solar light. Adsorption of nitrogen, scanning electron microscopy with energy-dispersive X-ray, temperature-programmed reduction, and X-ray diffraction characterization techniques were used in this work. Fe and Ni addition, as well as the different temperatures employed for calcination, have exercised influence over dyers photodiscoloration, which has come to 97% under artificial irradiation during a reaction time of 7 h and 75% with solar light during a reaction time of one hour. An artificial neural network (ANN) model known as radial basis function (RBF) has been proposed for the prediction of the photodiscoloration for reactive dye solutions. This paper also examines the comparison between the proposed model and two other different ANN models for the same task. The input parameters to the algorithm were dye reactive, light source, dopant metal, metallic charge, calcination temperature and reaction time, and the output was dye discoloration. The proposed RBF-ANN model efficiently predicted the discoloration. Its result in terms of root mean squared error was 92.0767%, which gave satisfactory results with the experimental data overcoming the other two models.

Keywords: Sol-gel method; Photocatalysis; Characterization; Radial basis function neural network

---

[*] Corresponding author.

1. Introduction

Prediction of the output water quality from an industrial wastewater treatment plant is a very hard task since the input water quality changes continuously, and this variation depends on many factors. One important advantage of the artificial neural network (ANN) model over classical techniques is that it does not require the complex nature of the underlying process. Based on experimental data, an ANN model, called radial basis function (RBF) was developed in this experiment. The RBF-ANN is a computational intelligence model inspired by the human brain. This model can be used for prior estimation of dye discoloration using an experimental dataset. The model was first trained using a partition of experimental data, and then, in order to validate the model, it was compared with the remaining partition of the dataset, in a 10-fold cross-validation way. Computational intelligence models have been applied successfully in various industrial wastewater treatment problems [1–4]. More recently, ANN regression models have been applied to these problems due to their pattern recognition capability correlating input and output variables. Jiang et al. [5] developed an ANN model for adsorption and photocatalysis of reactive dye on TiO_2 surface. They compared five different backpropagation functions using the correlation coefficient (R) as evaluation criterion, and obtained good results. Lenzi et al. [6] also applied an MLP model to photocatalytic degradation of textile reactive dye. Their evaluation criterion was the determination coefficient (R^2), and their results were good as well. On the other hand, Colpini et al. [7] proposed the application of a support vector regression (SVR) model to predict the capability of photodiscoloration of textile reactive dye, and also obtained good results in terms of root mean squared error (RMSE). In this paper, we propose the application of an RBF model in order to predict the textile reactive dye photodiscoloration, comparing the proposed model with MLP and SVR models under the same evaluation criterion: the RMSE. Works such as those by Ritter and Muñoz-Carpena [8] and Moriasi et al. [9], adopted by us as a theoretical reference in our work, use the RMSE as a criterion for determining the best model. Thereby, the three different models have been trained using the experimental data and tested to find the most suitable and reliable ANN model (although SVR is not exactly an ANN, it can be considered as such, because it is inspired by it (Vapnik) [10]. The ANN parameters (e.g., spreads, number of hidden layers, number of neurons in each hidden layer) for all models were found by trial and error method.

2. Materials and methods

2.1. Preparation of photocatalysts

The TiO_2, Fe/TiO_2, and Ni/TiO_2 catalysts were prepared by the sol-gel method using the molar ratio n_{water}:$n_{alkoxide}$:n_{acid} = 2.4:1:0.08 according to [11,12]. Titanium (IV) isopropoxide (≥97%, Sigma-Aldrich), Iron (III) nitrate nonahydrate (≥98%, Vetec) and Nickel nitrate hexahydrate (97%, Vetec) were used as metallic precursors.

In TiO_2 synthesis, two solutions were prepared under nitrogen atmosphere. Solution A was constituted by 15.00 mL of titanium (IV) isopropoxide and 22.80 mL of ethanol (≥95%, Cromate); Solution B was dissolved in 0.30 mL of nitric acid (≥70%, Vetec), 2.20 mL of doubly distilled water (resistivity ~13 MΩ cm) and 22.50 mL of ethanol. The two solutions were homogenized separately and stirred vigorously for 5 min. Solution B was added to Solution A by an addition funnel. The gel was formed up to 15 s, aged overnight and washed three times a day for 4 d with an acetone:water mixture (1:1). For Fe and Ni-doped TiO_2 synthesis, the Fe and Ni precursors were incorporated in Solution A in nominal loadings to obtain 2 and 5% wt, but these catalysts were not washed with an acetone:water mixture.

All the photocatalysts were dried in a rotating evaporator at 40°C–90°C for 1 h and later under a high vacuum (~10^{-3} atm) at 80°C for 8 h. Finally, the materials were calcined in a muffle at 250°C, 300°C and 400°C for 5 h.

2.2. Characterization of photocatalyst

The determination of the specific surface area (BET) of photocatalysts was performed through the physisorption of the N_2 method, using a Quantachrome Corporation (Nova 1200) equipment. Before the analysis, the samples were treated at 150°C for 2 h. The surface areas were based on a multipoint BET analysis.

An electronic scanning microscope (SEM), FEI Quanta 440 with microsound (EDS), was used in the analysis of the morphology of materials.

The TPR analysis was carried out on a homemade apparatus at 30 mL min^{-1} flow of 1.75% H_2 in Ar, a heating rate of 10°C min^{-1} to a final temperature of 1,000°C.

The X-ray diffraction patterns were measured through a Rigaku Geingerflex Diffractometer with Cu Kα radiation (λ = 0,154 nm), accelerating voltage of 45 kV and applied current of 25 mA.

2.3. Photocatalytic tests

The catalysts were applied on photodiscoloration of Orange-122, Blue-19 and Yellow-145 reactive dyes solutions (10 mg L^{-1}). All of these were purchased from Chemical Texpal Ltda (Valinhos, Brazil). The experiments were carried out by addicting 50 mg of catalyst in 150 mL of dye solution disposed on a 300 mL glass cylindrical photochemical reactor with magnetic stirring under both solar and artificial light (300 W tungsten UV lamp (Osram E27/ES, Ultra-Vitalux)).

After reaction time (1 h to solar light and 0.5–7.0 h to artificial light), the solids were separated from solutions by centrifugation (30 min at 3,400 rpm) and vacuum filtration with cellulose ester membranes (0.45 μm porosity). The discolorations rates were measured by external standardization on the highest absorption wavelength for each dye, and expressed as a percentage of discoloration. The average insolation of the solar irradiation (W/m^2) measured by an UV irradiance meter at the range of 390–1,100 nm (model LI-200, from SIMEPAR/Brazil) were 543–768, 755–781 and 656–755 to Yellow-145, Blue-19 and Orange-122, respectively.

2.4. ANN model development

Artificial neural network (ANN) is a machine learning technique inspired by the human brain. The idea of ANN as computational machines was introduced by McCulloch and Pitts (1943). According to Haykin [13], an ANN is a massively parallel distributed processor that has a natural propensity for storing experiential knowledge and making it available for use. It resembles the brain in two respects: (1) knowledge is acquired by the network through a learning process; and (2) interneuron connection strengths known as synaptic weights are used to store knowledge. ANN has a wide application field in several areas, like time series forecasting [14], medical diagnosis [15], computer vision [16], recommender system [17], systems identification [18], among others. ANN has been also used successfully for water treatment model development [5–7].

In this experiment, we applied RBF-ANN in order to predict the photodiscoloration of dyes reactive using the dataset generated by the experiments of photocatalytic tests. In this context, a RBF is an ANN that can be seen as a functions universal approximator, the basic idea is to find a function that best approaches the training data, minimizing prediction error. The RBF-ANN model, which had Powell [19] as pioneer researcher, is illustrated in Fig. 1, where x is the input layer composed by m dimensions, $\phi_i(x)$ is the hidden layer, w are the weights associated with the output layer, and b is the bias.

A generalized RBF-ANN model is applied in the present study. In this case, the learning problem can be simplified to determine the spreads of the radial basis functions (Gaussians) in the hidden layer. The larger the spread is, the smoother the function approximation. In other words, a larger spread means a lot of neurons are required to fit a fast-changing function, and a smaller spread means many neurons are required to fit a smooth function, and the network might not generalize well. In the present study, we tested different spreads in order to find the best value, varying this parameter between 10^{-4} and 10^{2} by trial-and-error method, and the best results were for spreads close to 10^{0}. The output layer has a pure linear transfer function, and both, hidden and output layers, have biases. The linear weights associated with the output layer, and the positions of the centers of radial-basis functions and the norm weighting matrix associated with the hidden layer have to be learned. The generalized RBF-ANN involves searching for suboptimal solution in a lower-dimensional space that approximates the regularized solution in Eq. (1).

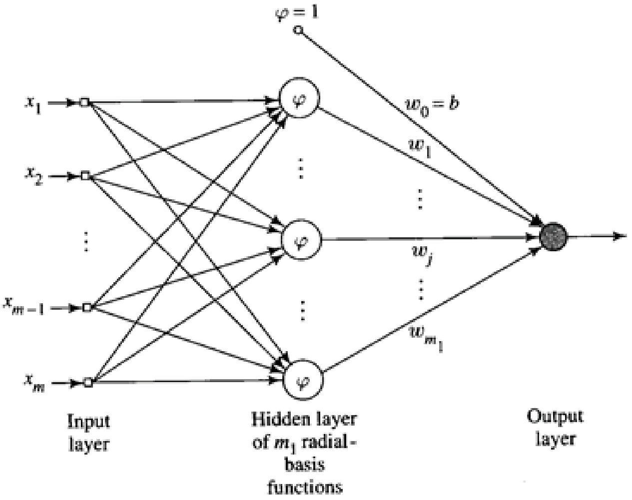

Fig. 1. RBF-ANN model.

$$F(x) = \sum_{i=1}^{m_1} w_i \varphi_i(x) \tag{1}$$

where $\{\varphi_i(x) \mid i = 1,2,...,m_1 \leq N\}$ is a new set of linearly independent basis functions and the w_i constitute a new set of weights.

Initially, the hidden layer had no neurons. The following steps are repeated until the network's mean squared error (MSE) falls below goal:

- The network is simulated;
- The input vector with the greatest error is found;
- A radial basis function neuron is added with weights equal to that vector; and
- The output layer weights are redesigned to minimize error.

After set up of the RBF-ANN, its results were compared with SVR and MLP-NN (using similar parameters of the applications in the above cited water waste treatment field papers) on the experimental data generated by the reactive dye photocatalysis process shown in this paper. MATLAB R2010a [20] was used to develop all models. More technical details of the ANN and RBF-ANN are described in [13,14].

The experimental dataset has 234 instances and 6 attributes (input variables). The input and output variables and the possible values for each variable (or ranges of values in case of continuous numerical variables) are given in Table 1. Data were normalized in such a way that the mean value of each feature is 0 and the standard deviation is 1.

The error rate adopted in this work is the RMSE), a frequently used measure of the difference between values predicted by a model and the values actually observed from the environment that is being modeled. These individual differences are also called residuals, and RMSE serves to aggregate them into a single measure of predictive power. The RMSE of a model prediction is an error rate with respect to the estimated variable $\hat{y}_i\hat{y}_i$, and it is defined as the square root of the MSE, according to Eq. (2):

$$\text{RMSE} = \sqrt{\frac{\sum_{i=1}^{n}\left(\hat{y}_i - y_i\right)^2}{n}} \tag{2}$$

where y_iy_i is observed values and $\hat{y}_i\hat{y}_i$ is predicted values at the ith term.

In order to be more intuitive, we adopted as evaluation criteria 1 – RMSE, which is the difference between a perfect prediction and the prediction error. One of the most common ways of predicting the error rate of a learning technique given a single, fixed sample of data is to use stratified 10-fold cross-validation, where "10-fold" means 10 partitions of the data and "stratified" means that stratification is adopted in the cross-validation. The data are divided randomly into 10 parts in which the class is represented in approximately the same proportion as in the full dataset. Each part

Table 1
Input and output variables and possible values

Variable	Type	Domain
Dye reactive	Input	Yellow–145, Orange-122, Blue-19
Light source	Input	Solar, Artificial
Dopant metal	Input	Fe, Ni, none
Metallic charge (%)	Input	0–5
Calcination temperature (°C)	Input	250–400
Reaction time (h)	Input	0.5–7
Dye discoloration (%)	Output	0–100

is held out in turn, and the learning scheme trained on the remaining 90%; then its error rate is calculated on the holdout set. Thus the learning procedure is executed a total of 10 times on different training sets (each of which have a lot in common). Finally, the 10 error estimates are averaged to yield an overall error estimate [21]. This whole validation process was applied for 100 iterations for each algorithm (RBF, MLP and SVR) in order to obtain the statistical results.

3. Results and discussion

3.1. Characterization

3.1.1. N_2 adsorption measurements

Fig. 2 presents the isotherms obtained by N_2 physisorption for calcined samples at the highest temperature, 400°C. The structure observed was the same for the remaining temperatures.

The observed isotherms were classified as type IV according to IUPAC, which is typical of mesoporous materials (20–500 Å) [22–24]. This is confirmed in Table 2, which presents the specific area for all materials.

Table 2 presents the results obtained for the specific surface area; with the raise in calcination temperature, it is perceivable that the specific area obtained was decreasing. Wu et al. [25], working with Ni/TiO_2 nanocomposites, ascribes the specific area decrease to TiO_2 matrix condensation and to pore collapse, claiming that such a decrease was more accentuated for TiO_2 without Ni, because the nanometric particles of the metal prevented pore collapse, offering support to TiO_2 walls. It was also observed that the raise in Ni and Fe metallic charge has caused a higher specific area [26].

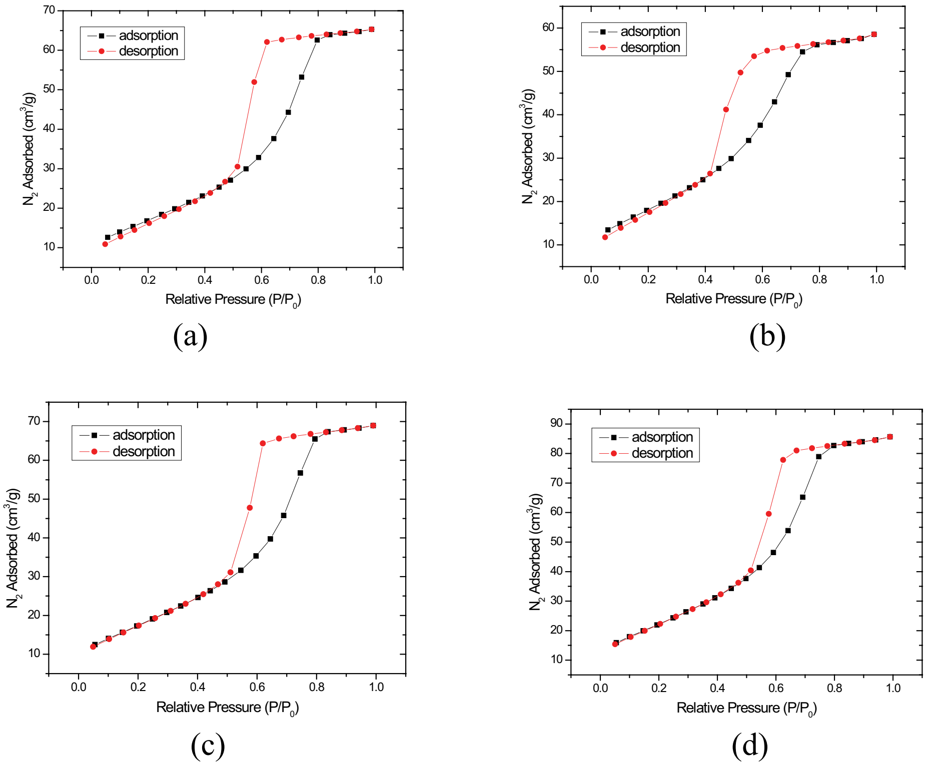

(a) (b) (c) (d)

Fig. 2. N_2 adsoption/desorption for the following materials: (a) 2% Fe/TiO_2 – 400°C, (b) 5% Fe/TiO_2 – 400°C, (c) 2% Ni/TiO_2 – 400°C and (d) 5% Ni/TiO_2 – 400°C.

Table 2
S_o values of the synthesized catalysts

Catalyst		
Fe and Ni (%wt)	Temperature calcination	S_o (m²/g)
2% Fe/TiO_2	non-calcined	215.42
	250°C	214.17
	300°C	135.15
	400°C	63.06
5% Fe/TiO_2	non-calcined	225.14
	250°C	257.96
	300°C	174.47
	400°C	67.83
2% Ni/TiO_2	non-calcined	295.42
	250°C	262.98
	300°C	227.76
	400°C	66.21
5% Ni/TiO_2	non-calcined	312.63
	250°C	300.95
	300°C	297.48
	400°C	84.41
TiO_2	non-calcined	329.40
	250°C	183.58
	300°C	145.25
	400°C	81.60

3.1.2. Scanning electron microscopy with energy-dispersive X-ray

Fig. 3 shows scanning electron micrographs obtained for Fe/TiO_2 and Ni/TiO_2, both calcined at 400°C.

It is observable in the SEM micrographs that the materials have extremely rough, porous, sponge-like surfaces, which texture has fundamentally influenced the high specific areas obtained. However, a part of the surface of the particles with spongy aspect is smooth and multifaceted, especially on the Ni/TiO_2 samples.

It is observable in Fig. 4b that Fe is uniformly distributed in the material, just as observed in Fig. 4d with Ni.

3.1.3. H_2 temperature-programmed reduction

Fig. 5 shows temperature-programmed reduction (TPR) patterns to the materials obtained.

It is observable for TiO_2 a reduction peak approximating 578°C, probably related to phase change from anatase-amorphous to more crystalline forms [27]. For Ni/TiO_2, two reduction peaks are observable in approximately 400°C and 576°C, related to Ni^{2+} to Ni^0 reduction [28,29]. It is likewise observable that there are two reduction peaks for the Fe/TiO_2 samples in approximately 380°C and 520°C related to Fe^{3+} to Fe^0 reduction [29,30]. The increase in massic proportion of Fe and Ni lead to an increase in H_2 consumption, which is to be expected, since there is more metal to be reduced.

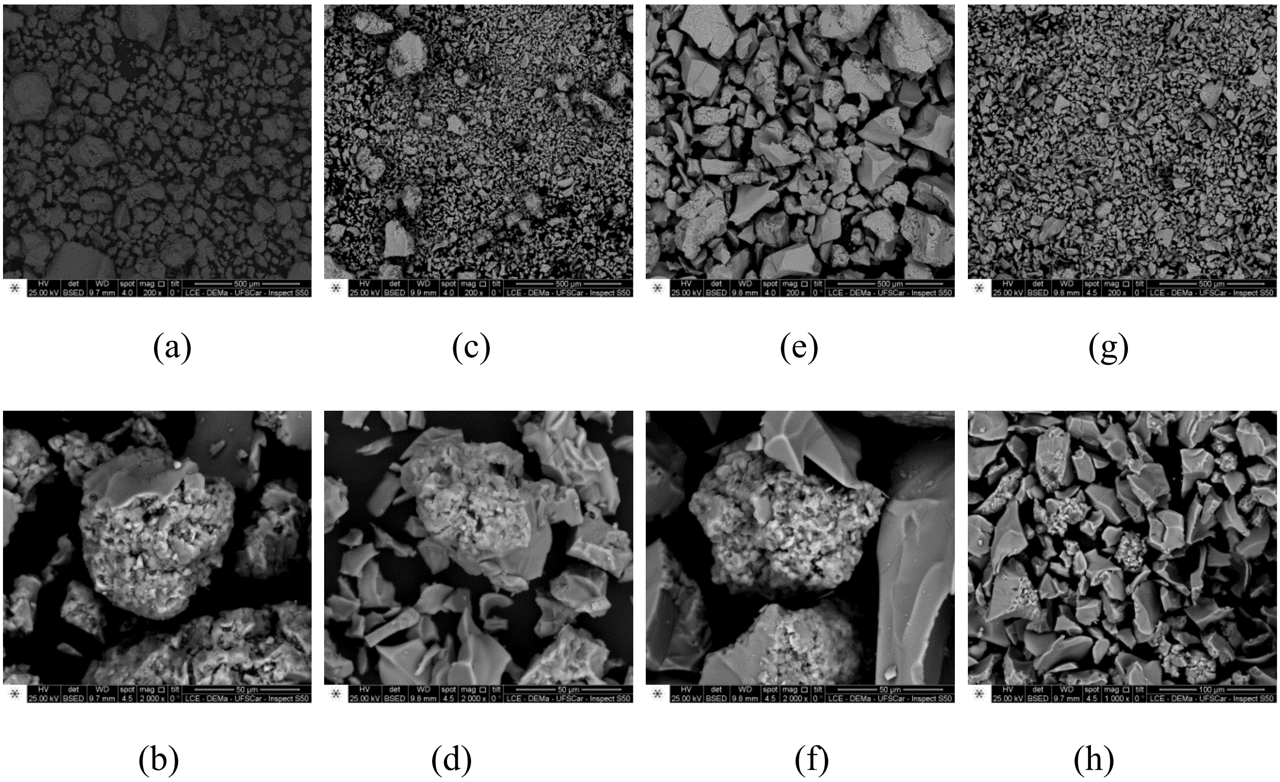

Fig. 3. Scanning electron micrographs for the following materials: (a) 2% Fe/TiO_2, amplification: 200x, (b) 2% Fe/TiO_2, amplification: 2,000x, (c) 5% Fe/TiO_2, amplification: 200x, (d) 5% Fe/TiO_2, amplification: 2,000x, (e) 2% Ni/TiO_2, amplification: 200x, (f) 2% Ni/TiO_2, amplification: 2,000x, (g) 5% Ni/TiO_2, amplification: 200x and (h) 5% Ni/TiO_2, amplification: 1,000x.

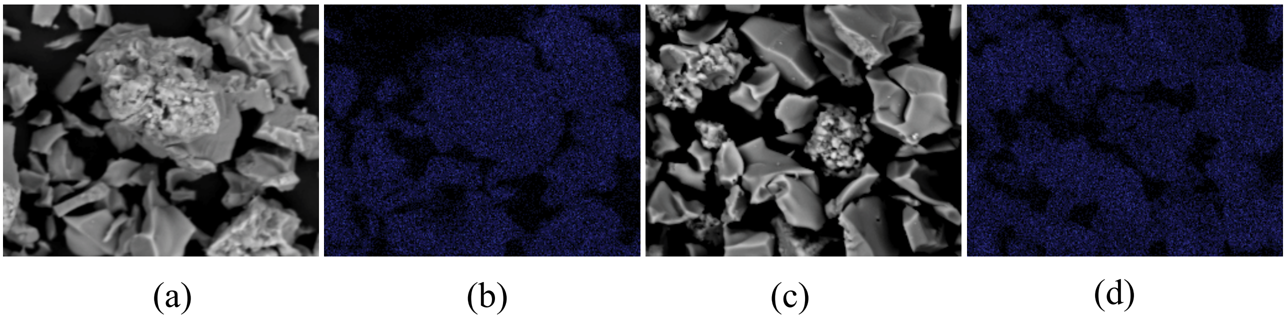

Fig. 4. Mapping in (b) of 5% Fe/TiO_2 exposed to (a) (amplification: 2,000x) and mapping in (d) of 5% Ni/TiO_2 exposed to (c) (amplification: 2,000x).

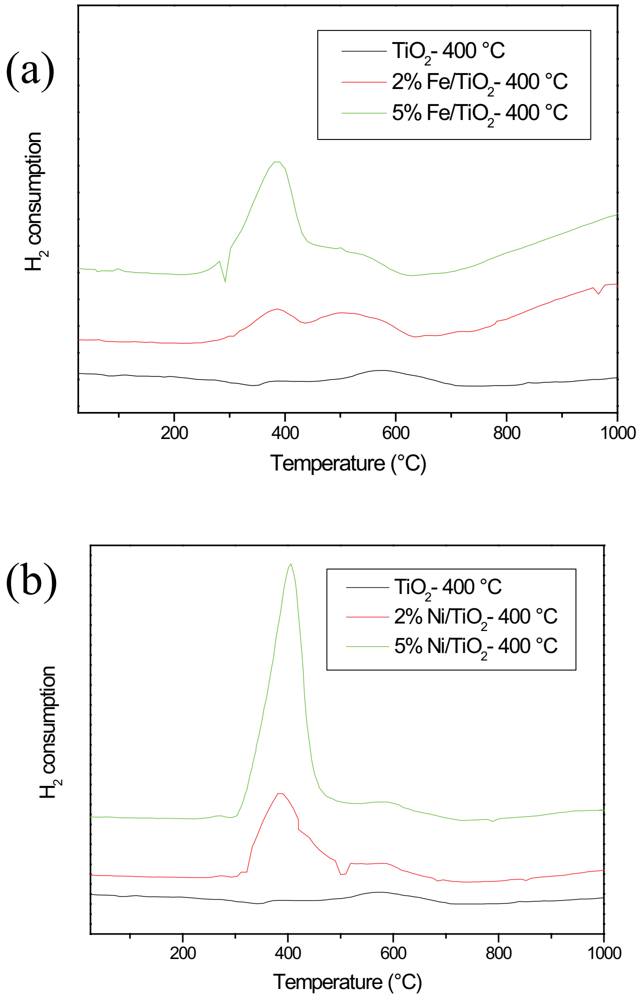

Fig. 5. TPR patterns for the following materials: (a) 2% Fe/TiO_2, 5% Fe/TiO_2 and TiO_2 and (b) 2% Ni/TiO_2, 5% Ni/TiO_2 and TiO_2, all calcined at 400°C.

3.1.4. X-ray diffraction

As observed in Fig. 6a and b, non-calcined materials do not present crystallization peaks, regardless of massic proportion and of the metal used, being classified as amorphous. All materials, except non-calcined Fe/TiO_2 and Ni/TiO_2, and including TiO_2 materials presented in Fig. 7, present peaks related to the presence of a crystalline TiO_2 phase in anatase form, and do not show peaks related to other TiO_2 crystalline phases, such as rutile and brookite. This fact is probably related to low calcination temperature and to a rise in TiO_2 stability when in anatase form, provided by Ni incorporation [26,31,32]. On the other hand, the relevant literature shows that Fe incorporation would lower the transformation temperature from anatase to rutile, that was not observed [33,34].

For both Fe and Ni, corresponding crystalline phases where observed, due to their high dispersion. On the other hand, Fe^{3+} ions have a ratio approximate to the ratio of Ti^{4+} (0.64 and 0.68 Å, respectively), infiltrating into the TiO_2 structure by cation substitution [33–36]. Besides, Fe^{3+} ions may lodge in the interstices of the TiO_2 network, and in defects caused by the difference in the introduced Fe^{3+} ratio [33,37]. Likewise, studies show that Ni^{2+} ions may also infiltrate into the TiO_2 structure, and thus become non-detectable by diphratograms [26,31].

3.2. Photocatalytic essays

Table 3 shows discoloration results for the following dyes solutions: Yellow-145, Blue-19 and Orange-122, when assisted by solar time for the reaction time of one hour.

It is observable that, in most cases, the 400°C calcination temperature has become more efficient in discoloration, with the exception of TiO_2. As for the catalysts calcined at 400°C, it is evident that the increase in Fe and Ni massic proportion from 2% to 5% entailed an increase in discoloration, with the exception of Fe/TiO_2 when applied to dye Orange-122. However, synthetized materials Fe/TiO_2 and Ni/TiO_2 did not present discoloration rates more efficient than TiO_2.

Fig. 8 and Table 4 present discoloration obtained when reactions were assisted by artificial light.

As observed in the essays under solar light, catalysts Fe/TiO_2 and Ni/TiO_2, calcined at 400°C, show more efficiency; the same is observable under artificial light, reaching approximately 97% discoloration and using 5% Ni/TiO_2 for Yellow-145 and 2% Ni/TiO_2 for Orange-122. On the other hand, the same was not observed when TiO_2 was used (Table 4), with calcination at 250°C being most favorable for Blue-19 and Orange-122 and 300°C for Yellow-145.

Even with smaller reaction times, better discoloration rates were observed when TiO_2 was used, reaching 100%

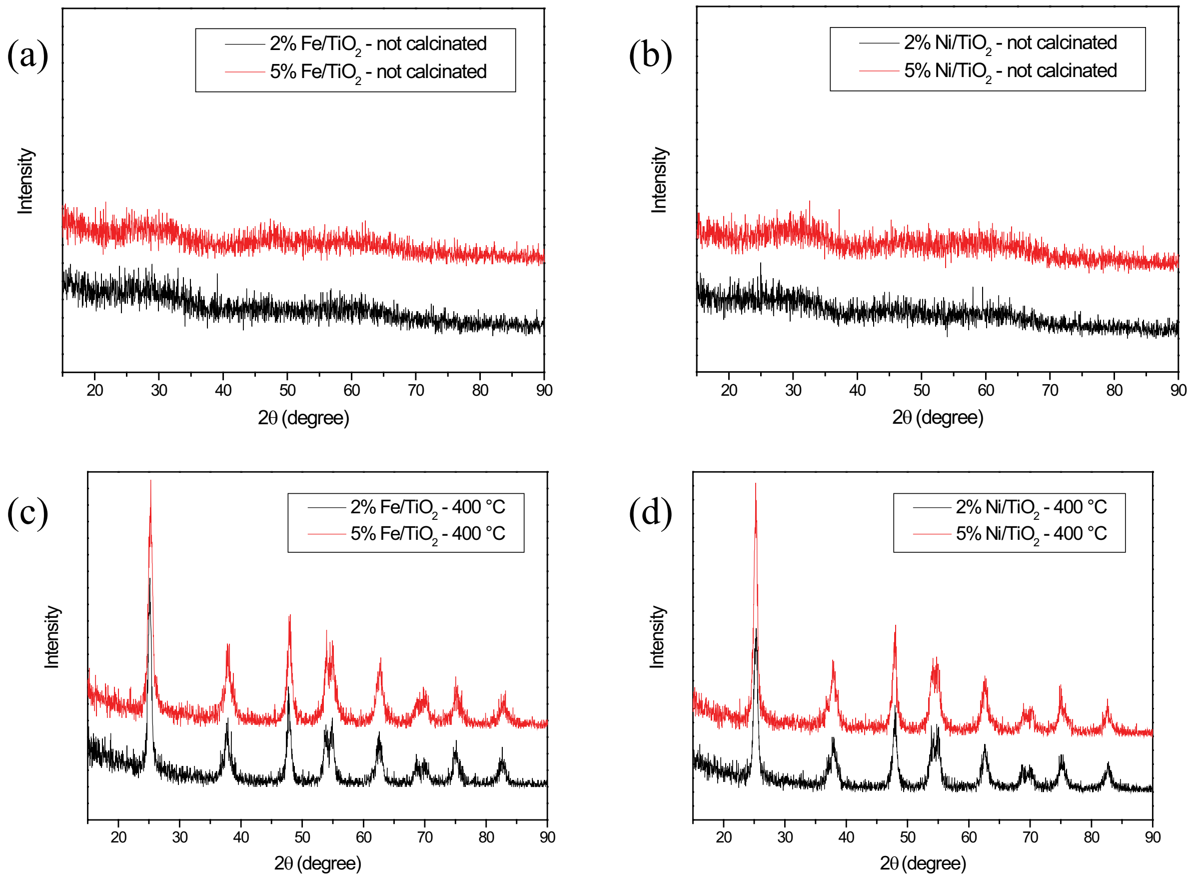

Fig. 6. Diphratograms obtained for the following materials: (a) Fe/TiO$_2$ and (b) Ni/TiO$_2$, both non-calcined, (c) Fe/TiO$_2$ and (d) Ni/TiO$_2$, calcined at 400°C.

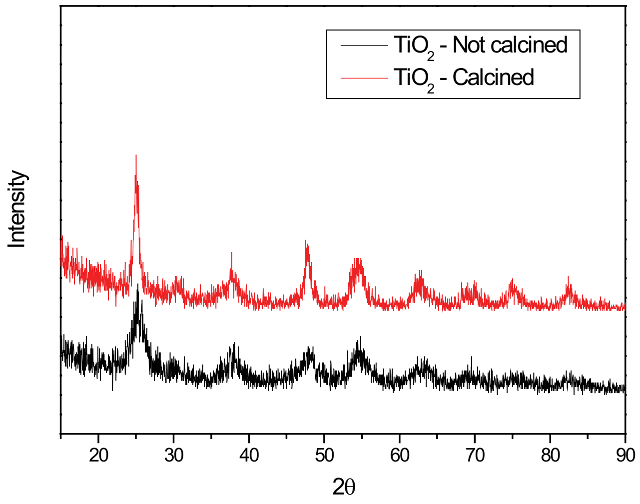

Fig. 7. Diphratograms obtained for TiO$_2$, non-calcined and calcined at 400°C.

discoloration in 2 h, when calcined at 250°C with dye Orange-122.

Contrary to what occurred in the solar light essays, the 2% mass percentage of metal incorporation was observed to be more efficient in Orange-122, this was not observed for Yellow-145 and Blue-19; it showed efficiency with these sometimes at 2%, sometimes at 5%. This is possibly due to the difference in the structure of the dyes. However, calcination temperature exerts great influence in dyes discoloration.

3.3. Artificial neural network model

The best RMSE of RBF on the dataset was 92.0767%, this is a very good result with the experimental data, against 66.9838% of MLP and 88.5187% of SVR. Table 5 shows the results (comparison) for the photocatalytic discoloration models. Actually, RBF defeats MLP and SVR in all statistics of RMSE (best, worst, average and standard deviation), especially against MLP. Another advantage of RBF is its computational performance (in minutes and seconds). It had a better performance than both other models in terms of computational processing cost, overcoming significantly even (and notably) the SVR, the model that presented the closest performance of the RBF in terms of RMSE statistics.

Figs. 9, 10 and 11 illustrate these results for RBF, MLP and SVR models, respectively, for an example test fold of one full cross-validation iteration for each model. Each graph represents one of the ten test folds, where the *x*-axis shows the numbers of each test instance for the fold and the

Table 3
Dyes solutions discoloration under solar light (reaction time: 1 h)

Catalyst	Discoloration (%)		
	Yellow-145	Blue-19	Orange-122
2% Fe/TiO_2 - 250°C	13.10	1.66	2.02
2% Fe/TiO_2 - 300°C	4.40	12.54	9.33
2% Fe/TiO_2 - 400°C	27.60	15.88	56.97
5% Fe/TiO_2 - 250°C	0.00	1.66	3.55
5% Fe/TiO_2 - 300°C	3.55	4.18	2.45
5% Fe/TiO_2 - 400°C	46.30	25.92	54.03
2% Ni/TiO_2 - 250°C	10.49	4.92	10.72
2% Ni/TiO_2 - 300°C	0.00	0.00	1.47
2% Ni/TiO_2 - 400°C	19.19	16.72	33.40
5% Ni/TiO_2 - 250°C	6.14	6.55	3.55
5% Ni/TiO_2 - 300°C	0.92	1.67	0.00
5% Ni/TiO_2 - 400°C	33.83	44.31	75.15
TiO_2 - 250°C	78.34	65.26	70.65
TiO_2 - 300°C	86.17	65.22	100.00
TiO_2 - 400°C	85.30	51.84	100.00

y-axis presents the dye discoloration in %. The blue points are the observed discoloration, the red points are the predicted discoloration by the respective model and the black line is the mean of observed discoloration. The proximity between predicted and observed points explains the good results for RMSE.

Table 4
Dyes solutions discoloration (%) with TiO_2 (reaction time: 2 h)

Dye	Catalyst	Discoloration (%)
Yellow-145	TiO_2 - 250°C	78.83
	TiO_2 - 300°C	96.26
	TiO_2 - 400°C	94.6
Blue-19	TiO_2 - 250°C	90.09
	TiO_2 - 300°C	52.42
	TiO_2 - 400°C	47.51
Orange-122	TiO_2 - 250°C	100.00
	TiO_2 - 300°C	96.24
	TiO_2 - 400°C	91.69

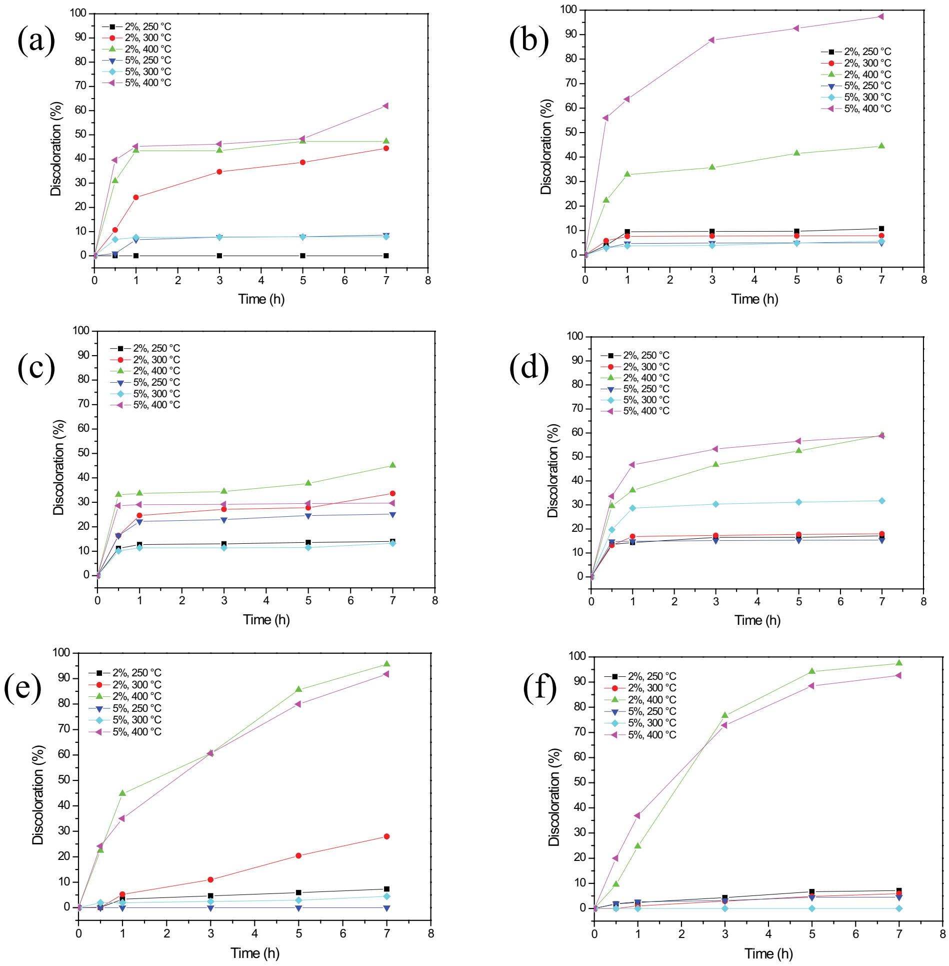

Fig. 8. Discoloration as a function of time for the following materials: Fe/TiO_2 for dye Yellow-145 in (a), Blue-19 in (c) and Orange-122 in (e), Ni/TiO_2 for dye Yellow-145 in (b), Blue-19 in (d) and Orange-122 in (f).

Table 5
Comparative analysis of ANN models

Model	RMSE (%)				Computational cost
	Best	Worst	Average	Standard deviation	
RBF	92.0767	90.0155	90.8495	0.5238	13′58″
MLP	66.9838	46.7654	57.8733	5.9769	15′54″
SVR	88.5187	85.4008	87.2218	1.0393	46′41″

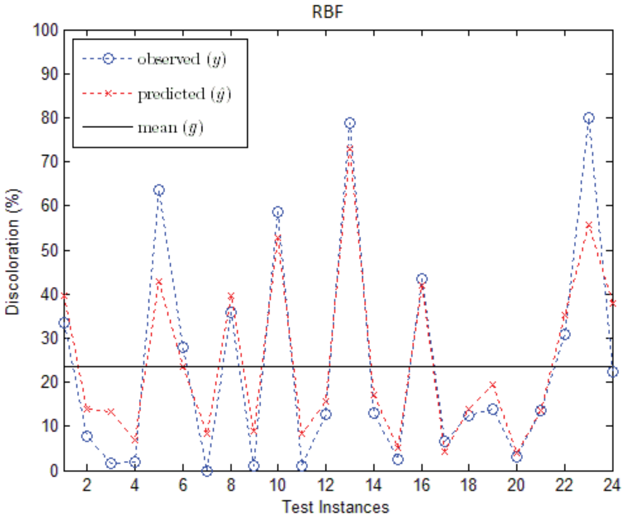

Fig. 9. RBF model discoloration.

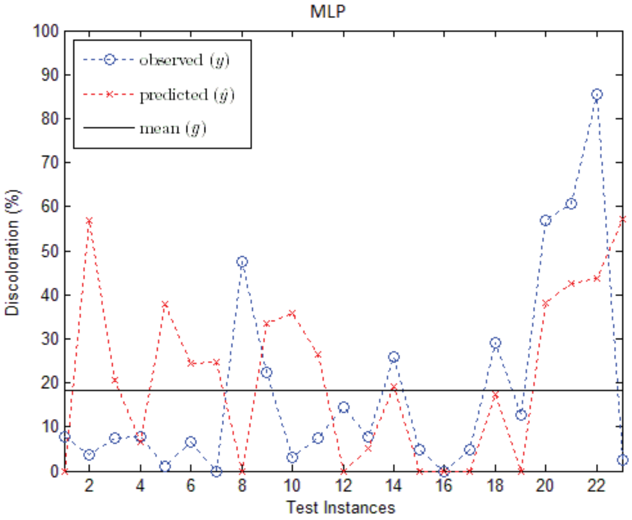

Fig. 10. MLP model discoloration.

4. Conclusions

Given the results obtained in the photocatalytic essays conducted, it was observed that the addition of Fe and Ni to titania, as well as the calcination the temperatures used, exert influence on photodiscoloration of dyes solutions Yellow-145, Blue-19 and Orange-122. Generally, calcination

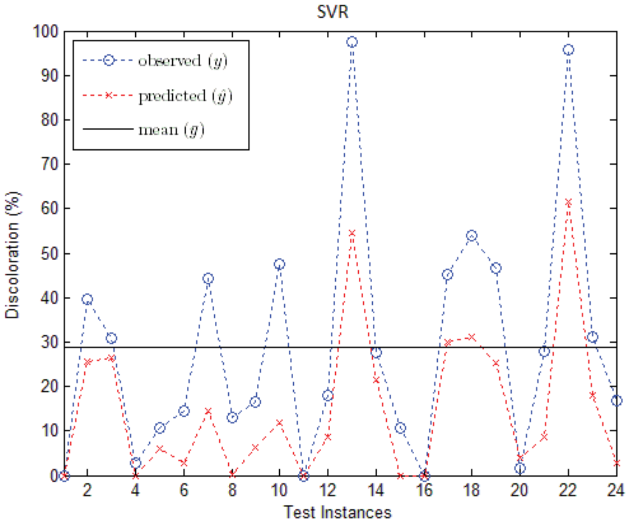

Fig. 11. SVR model discoloration.

temperature at 400°C has shown more efficiency when materials Fe/TiO_2 and Ni/TiO_2 were used.

The rigorous comparative study of ANN models for photocatalysis shows that the finding of a reliable network model is a vital job. The proposed generalized RBF-ANN model performs a proper previous checking before applying to any real photocatalytic degradation process. The effectiveness of this model to deal with the machine learning task in a simple and fast way makes it an extremely useful tool for prediction of the reactive dye discoloration. Its simplicity is related to its capacity to deal with the variation in the experimental dataset without any other information about the complex nature of the discoloration process, and just tuning of a single ANN parameter: the spread of radial basis functions. In a future work, we intend to apply an optimization algorithm for tuning the spread parameter to solve the same problem.

Acknowledgments

The authors would like to thank the Fundação Araucária for the financial support of this study and Simepar by insolation data of the solar irradiation.

References

[1] Y.M. Slokar, J. Zupan, A.M. Le Marechal, The use of artificial neural network (ANN) for modeling of the H_2O_2/UV decoloration process: part I, Dyes Pigm., 42 (1999) 123–135.

[2] D. Salari, N. Daneshvar, F. Aghazadeh, A.R. Khataee, Application of artificial neural networks for modeling of the treatment of wastewater contaminated with methyl tert-butyl ether (MTBE) by UV/H_2O_2 process, J. Hazard Mater., 125 (2005) 205–210.

[3] J.C. Chen, N.B. Chang, Mining the fuzzy control rules of aeration in a submerged biofilm wastewater treatment process, Eng. Appl. Artif. Intell., 20 (2007) 959–969.

[4] O.L.C. Guimarães, M.H.R. Chagas, D.N. Villela Filho, A.F. Siqueira, H.J. Izario Filho, H.O.Q. Aquino, M.B. Silva, Discoloration process modeling by neural network, Chem. Eng. J. Lausanne, 140 (2008) 71–76.

[5] Z. Jiang, J. Hu, X. Zhang, Y. Zhao, X Fan, S. Zhong, H. Zhang, X. Yua, A generalized predictive model for TiO_2–Catalyzed photo-degradation rate constants of water contaminants through artificial neural network, Environ. Res., 187 (2020) 109697, doi: 10.1016/j.envres.2020.109697.

[6] G.G. Lenzi, R.F. Evangelista, E.R. Duarte, L.M.S. Colpini, A.C. Fornari, R. Menechini Neto, LMM. Jorge, O.A.A. Santos, Photocatalytic degradation of textile reactive dye using artificial neural network modeling approach, Desal. Water Treat., 57 (2015) 14132–14144.

[7] L.M.S. Colpini, G.G. Lenzi, R.C. Thom de Souza, M.B. Urio, D.M. Kochepka, M.A.R. Santos, E.C. Vasques, H.J. Alves, Photodiscoloration processes of dyes reactive using radiation and Fe/TiO_2, Int. J. Mater. Eng. Technol., 16 (2016) 189–204.

[8] A. Ritter, R. Muñoz-Carpena, Performance evaluation of hydrological models: statistical significance for reducing subjectivity in goodness-of-fit assessments, J. Hydrol., 480 (2013) 33–45.

[9] D.N. Moriasi, J.G. Arnold, M.W. Van Liew, R.L. Bingner, R.D. Harmel, T.L. Veith, Model evaluation guidelines for systematic quantification of accuracy in watershed simulations, Trans. ASAE, 50 (2007) 885–900.

[10] V.N. Vapnik, The Nature of Statistical Learning, Springer, New York, 1995.

[11] L.M.S. Colpini, H.J. Alves, O.A.A. Santos, C.M.M. Costa, Discoloration and degradation of textile dye aqueous solutions with titanium oxide catalysts obtained by the sol–gel method, Dyes Pigm., 76 (2008) 525–529.

[12] G.G. Lenzi, M.K. Lenzi, M.L. Baesso, A.C. Bento, L.M.M. Jorge, O.A.A. Santos, Cobalt, nickel and ruthenium-silica based materials synthesized by the sol-gel method, J. Non-Cryst. Solids, 354 (2008) 4811–4815.

[13] S.S. Haykin, Neural Networks: A Comprehensive Foundation, 2nd ed., Prentice-Hall, New Jersey, 1998.

[14] R.C. Thom de Souza, Previsão de séries temporais utilizando rede neural treinada por filtro de Kalman e evolução diferencial, Master's Dissertation, Pontifical University Catholic of Paraná, Brazil, 2008.

[15] J. Li, Y. Ping, H. Li, H. Li, Y. Liu, B. Liu, Y. Wang, Prognostic prediction of carcinoma by a differential-regulatory-network-embedded deep neural network, Comput. Biol. Chem., 88 (2020) 107317, doi: 10.1016/j.compbiolchem.2020.107317.

[16] R. Zhang, Q. Zong, L. Dou, X. Zhao, Y. Tang, Z. Li, Hybrid deep neural network using transfer learning for EEG motor imagery decoding, Biomed. Signal Process. Control, 63 (2021) 102144, doi: 10.1016/j.bspc.2020.102144.

[17] M. Gridacha, Hybrid deep neural networks for recommender systems, Neurocomputing, 413 (2020) 23–30.

[18] L.S. Coelho, R.C. Thom de Souza, Identificação do Processo Experimental Bola e Tubo usando Rede Neural e Otimização Baseada em uma Abordagem Caótica de Evolução Diferencial, Congresso Brasileiro de Automática - Proceedings, Juiz de Fora, Brazil, 2008.

[19] M.J.D. Powel, Radial Basis Function Approximations to Polynomials, Numerical Analysis 1987 Proceedings, Dundee, 1988, pp. 223–241.

[20] The Mathworks, 2017. Available at: http://www.mathworks.com

[21] I.H. Witten, E. Frank, Data Mining – Practical Machine Learning Tools and Techniques, 2nd ed, Morgan Kaufmann, San Francisco, 2005.

[22] M. Sawangphruk, P. Srimuk, P. Chiochan, A. Krittaya-vathananon, S. Luanwuthi, J. Limtrakul, High-performance supercapacitor of manganese oxide/reduced graphene oxide nanocomposite coated on flexible carbon fiber paper, Carbon, 60 (2013) 109–116.

[23] M. Trejda, A. Tuel, J. Kujawa, B. Kilos, M. Ziolek, Niobium rich SBA-15 materials–preparation, characterization and catalytic activity, Microporous Mesoporous Mater., 110 (2008) 271–278.

[24] D.R. Amgarten, Determinação do volume específico de poros de sílicas cromatográficas por dessorção de líquidos em excesso, Master's Dissertation, University State of Campinas, Brazil, 2006.

[25] Y. Wu, X. Wu, L. Zhang, Preparation and microstructure characterization of Ni/TiO_2 nanocomposite, China Part., 1 (2003) 262–265.

[26] M.A. Ahmed, Synthesis and structural features of mesoporous NiO/TiO_2 nanocomposites prepared by sol–gel method for photodegradation of methylene blue dye, J. Photochem. Photobiol., A, 238 (2012) 63–70.

[27] J. Keränen, A. Auroux, S. Ek-Harkonen, L. Niinisto, Calorimetric measurements of the acidity of supported vanadium oxides prepared by ALE and impregnation, Thermochim. Acta, 379 (2001) 233–239.

[28] T. Wu, Q. Yan, H. Wan, Partial oxidation of methane to hydrogen and carbon monoxide over a Ni/TiO_2 catalyst, J. Mol. Catal. A: Chem., 226 (2005) 41–48.

[29] S.N.R. Inturi, S.N.R. Inturi, T. Boningari, M. Suidan, P.G. Smirniotis, Visible-light-induced photodegradation of gas phase acetonitrile using aerosol-made transition metal (V, Cr, Fe, Co, Mn, Mo, Ni, Cu, Y,Ce, and Zr) doped TiO_2, Appl. Catal. B., 144 (2014) 333 –342.

[30] S.C. Roy, H.L. Prasad, P. Dutta, A. Bhattacharya, B. Singh, S. Kumar, V.K. Kaushik, S.M. Pillai, M. Ravindranathan, Conversion of syn-gas to lower alkenes over Fe-TiO_2-ZnO-K_2O catalyst system, Appl. Catal. A, 220 (2001) 153–164.

[31] Y. Wan, B. Sun, Z. Xu, W. Chao, Effect of UV irradiation on wear protection of TiO_2 and Ni-doped TiO_2 coatings, Appl. Surf. Sci., 258 (2012) 4347–4350.

[32] N. Bahadur, R. Pasricha, G.S. Chand, R.K. Kotnala, Effect of Ni doping on the microstructure and high Curie temperature ferromagnetism in sol–gel derived titania powders, Mater. Chem. Phys., 133 (2012) 471–479.

[33] W.C. Hung, Y.C. Chen, H. Chu, T.K. Tseng, Synthesis and characterization of TiO_2 and Fe/TiO_2 nanoparticles and their performance for photocatalytic degradation of 1,2-dichloroethane, Appl. Surf. Sci., 255 (2008) 2205–2213.

[34] W. Hung, S. Fu, J. Tseng, H. Chu, T. Ko, Study on photocatalytic degradation of gaseous dichloromethane using pure and iron ion-doped TiO_2 prepared by the sol–gel method, Chemosphere, 66 (2007) 2142–2151.

[35] H. Meng, B. Wang, S. Liu, R. Jiang, H. Long, Hydrothermal preparation, characterization and photocatalytic activity of TiO_2/Fe–TiO_2 composite catalysts, Ceram. Int., 39 (2013) 5785–5793.

[36] J. Zhu, F. Chen, J. Zhang, H. Chen, M. Anpo, Fe^{3+}-TiO_2 photocatalysts prepared by combining sol–gel method with hydrothermal treatment and their characterization, J. Photochem. Photobiol. A, 180 (2006) 196–204.

[37] J.A. Wang, R.L. Ballesteros, T. López, A. Moreno, R. Gómez, O. Novaro, X. Bokhimi, Quantitative determination of titanium lattice defects and solid-state reaction mechanism in Iron-doped TiO_2 photocatalysts, J. Phys. Chem. B, 105 (2001) 9692–9698.